



Eksploracja i Niezawodność – Maintenance and Reliability

Volume 28 (2026), Issue 1

journal homepage: <http://www.ein.org.pl>

Article citation info:

Rymarczyk T, Kulisz M, Kłosowski G, Wójcik D, Kowalski M, Król K, Improving the reliability of industrial reactors by using differential neural network architecture in ultrasonic tomography, *Eksploracja i Niezawodność – Maintenance and Reliability* 2026; 28(1) <http://doi.org/10.17531/ein/208883>

Improving the reliability of industrial reactors by using differential neural network architecture in ultrasonic tomography

Indexed by:



Tomasz Rymarczyk^{a,b,*}, Monika Kulisz^c, Grzegorz Kłosowski^c, Dariusz Wójcik^{a,b}, Marcin Kowalski^a, Krzysztof Król^{a,b}

^a WSEI University, Poland

^b Research and Development Center, Netrix S.A., Poland

^c Lublin University of Technology, Poland

Highlights

- Innovative neural network structure with a differential layer.
- A universal method suitable for various types of neural networks.
- Achieved sharper reconstructions with enhanced structural detail and fidelity.
- Validated on real-world reactor data using a 16-transducer UST system.
- Suitable for industrial monitoring under limited and noisy measurement conditions.

Abstract

Ultrasonic tomography (UST) represents a powerful non-invasive diagnostic technique for monitoring and analyzing internal processes within industrial reactors. Despite its potential, UST-based reconstructions are often challenged by the ill-posed nature of the inverse problem, limited measurements, and the presence of noise. To address these limitations, this study introduces a novel differential neural network architecture that enhances conventional deep learning models by incorporating a specialized differential layer. This layer processes two parallel input streams and operates on their residuals, thereby amplifying subtle variations in the data critical for accurate tomographic reconstructions. This study aims to empirically validate the concept of the efficacy of differentiated architecture. Reconstruction performance was evaluated using established quantitative metrics. Results demonstrate that models incorporating the differential layer consistently outperform their standard counterparts, delivering higher resolution, improved structural integrity, and superior noise robustness. The universality and efficiency of the differential architecture across both sequential and spatial models highlight its applicability to a wide range of inverse imaging problems in industrial settings.

Keywords

industrial reactors, ultrasound tomography, neural networks, machine learning

This is an open access article under the CC BY license (<https://creativecommons.org/licenses/by/4.0/>)

1. Introduction

Tomography is a group of imaging techniques that allow non-invasive analysis of the internal structure of objects and systems. Tomographic techniques used in nondestructive testing include electrical impedance tomography (EIT), electrical capacitance tomography (ECT), ultrasonic tomography (UST), optical tomography (OT), and X-ray computed tomography. EIT is

based on the measurement of the electrical conductivity of the object to be examined and is used in medicine and the study of conductive materials [20, 27]. ECT uses the measurement of electrical capacitance between electrodes, which is useful in the analysis of multiphase flows and chemical processes [15, 39, 40]. UST, on the other hand, is based on the propagation of

(*) Corresponding author.

E-mail addresses:

T. Rymarczyk (ORCID: 0000-0002-3524-9151) tomasz@rymarczyk.com, M. Kulisz (ORCID: 0000-0002-8111-2316) m.kulisz@pollub.pl, G. Kłosowski (ORCID: 0000-0001-7927-3674) g.klosowski@pollub.pl, D. Wójcik (ORCID: 0000-0002-4200-3432) dariusz.wojcik@wsei.pl, M. Kowalski (ORCID: 0000-0002-1644-0612) marcin.kowalski@wsei.pl, K. Król (ORCID: 0000-0002-0114-2794) krzysztof.król@netrix.com.pl,

ultrasonic waves through the medium under test, providing detailed information on the structure and properties of the object [3, 4]. Optical tomography encompasses a range of imaging techniques that use light to non-invasively examine the internal structure of objects. One prominent type, optical coherence tomography (OCT), provides high-resolution cross-sectional images and is widely used in ophthalmology, dermatology, cardiology, and materials science for microstructure analysis [11, 16, 30]. X-ray computed tomography employs X-rays to generate detailed cross-sectional images of an object. It is widely used in medical diagnostics, industrial inspection, and material analysis, providing high-resolution imaging of internal structures without the need for physical sectioning [22, 45]. These various tomographic techniques enable researchers and engineers to analyze internal structures non-invasively, each method being suited to specific materials, environments, and applications.

UST is an effective, non-intrusive imaging method extensively utilized in industrial settings to observe the internal structures of reactors and fluid environments [8, 37]. It is essential in guaranteeing operational safety, enhancing processes, and identifying irregularities in different industrial systems. Through the examination of ultrasonic wave propagation within a medium, UST allows for the reconstruction of spatial distributions of acoustic parameters, providing important understanding of the internal conditions of industrial reactors [17].

By passing high-frequency ultrasonic waves through an industrial process medium and monitoring how their behavior changes as they travel, UST operates. The physical and chemical characteristics of the medium these waves travel through determine whether they are transmitted, reflected, refracted, or scattered [23, 38]. The way these waves interact with their environment is significantly influenced by factors such as the material composition, flow dynamics, and structural imperfections inside reactors, pipelines, or pressure containers [25]. Without having physical access to the system, UST makes it possible to recreate intricate representations that show interior conditions by recording and processing these interactions.

UST can be used in industry for monitoring multiphase flow dynamics, where gas-liquid and solid-liquid interactions affect efficiency. Visualizing and quantifying phase distribution, flow

patterns, and turbulence help engineers improve process performance and resolve inefficiencies [21, 24]. Image-based tomographic techniques have also been applied to investigate the dynamic behavior of gas bubbles, providing complementary insights into local flow parameters and spatial characteristics [31]. In addition to improving process control, tracking is important for preventing failures and making processes better. Preventing machine problems is important because they can stop production. UST helps lower these risks and makes processes more efficient by finding problems in how things flow.

UST is also useful for finding structural damage in essential structures like pressure vessels, pipelines, and reactors. These structures experience harsh conditions over time, which can lead to rust, wear and tear, and even cracks [5, 6]. By enabling predictive maintenance and lowering the chance of catastrophic failure, UST offers a non-invasive way to identify these flaws early [12, 26, 36]. In addition to its important role in preventing failures, tomography is a major contributor to process optimization. It helps enterprises to improve productivity on a number of levels by providing real-time information regarding turbulence and phase interactions. Through the reduction of cycles, the reduction of material consumption, and the enhancement of automation in process control, these insights help to minimize production costs. These enhancements subsequently facilitate the advancement of high-performance, sustainable, and cost-effective industrial operations [13, 18, 33].

UST is important in the analysis of fluid mixing processes in industrial systems. Numerous chemical reactions and material processing operations necessitate uniform mixing to guarantee product consistency and optimize yield [47]. UST allows engineers to assess mixing efficiency and make real-time adjustments by visualizing the flow and dispersion of components. It delivers feedback on critical parameters like temperature, density, and phase distribution, maintaining process stability. Monitoring and controlling these parameters in real time enhances decision-making, safety, and process optimization [1, 2].

The use of deep learning methodologies, specifically convolutional neural networks (CNNs) [14, 29, 34] and long short-term memory (LSTM) networks [10, 44, 46], has resulted in a transformative change in ultrasonic tomography (UST) by markedly improving image reconstruction, defect identification,

and process oversight. Traditional tomographic techniques often struggle with the inverse problem due to limited measurement availability, which hinders the achievement of high-resolution imaging [7]. CNNs, designed to autonomously extract spatial characteristics from pictures, have become a crucial tool in improving tomographic reconstruction by optimizing edge detection, reducing artifacts, and increasing noise resilience. By leveraging multiple convolutional layers, these networks have the capacity to discern intricate patterns in ultrasonic signals, thereby facilitating more precise phase distribution analysis in multiphase flow monitoring and structural integrity assessments.

The combination of CNNs with wavelet transformations has been shown to effectively suppress noise and enhance edge detection in images. This method captures intricate local characteristics and minimizes background noise, leading to crisper and more accurate edge maps [43]. The integration of adaptive variational mode decomposition with CNNs has demonstrated high accuracy in denoising ultrasonic signals, achieving an accuracy rate of 93.94% in distinguishing different signal-to-noise ratio combinations [41]. Convolutional neural networks have been utilized for effective noise filtering and the reduction of prevalent artifacts, including shadowing and reverberation in ultrasonic images, thereby enhancing image fidelity and spatial resolution [42]. Enhanced CNN architectures that incorporate attention mechanisms and encoder-decoder structures improve the resolution of low-frequency ultrasonic images while preserving structural and textural information, thereby enhancing edge contour definition [19].

LSTM networks, on the other hand, are particularly effective in handling sequential UST data, making them well-suited for applications that require tracking changes over time. Given that industrial UST is frequently employed for real-time monitoring of dynamic processes, such as the detection of flow instabilities in pipelines or gradual material degradation, LSTMs are capable of analyzing temporal dependencies in ultrasonic signals. This feature facilitates enhanced trend analysis, anomaly detection, and predictive maintenance, assuring the identification of structural flaws before they escalate into significant breakdowns. Engineers can predict future system behavior by training LSTMs using previous records, facilitating the

optimization of operational parameters and the avoidance of expensive downtime [9].

The utilization of bidirectional LSTM networks alongside automatic alignment methods has been shown to enhance the precision and efficacy of equipment monitoring [28]. In the context of oil and gas pipelines, LSTMs optimized with the dung beetle optimization algorithm have been shown to enhance detection accuracy and reduce detection time, thereby demonstrating the model's capacity for rapid and precise classification of pipeline data features [35]. Furthermore, LSTM networks in conjunction with autoencoders have been employed for the purpose of leak detection within water supply systems [32].

The progress in the field of UST, especially with the incorporation of neural networks like CNN and LSTM, has resulted in significant improvements in the quality of image reconstruction. This advancement has enabled a more precise representation of the internal parameters of the examined structures. However, tomographic reconstruction has considerable difficulties because of the limited number of input data, the impact of measurement noise, and the occurrence of artifacts that might undermine the precision of the outcomes. Therefore, it is necessary to constantly improve computational methods that will increase precision and robustness to noise.

1.2. Motivation, novelty and paper structure

The reconstruction of internal structures in industrial systems via ultrasonic tomography (UST) poses significant challenges owing to the intrinsic boundaries of inverse issues. The limitations generally arise from the limited availability of measurements, the existence of noise, and the difficulty in obtaining high-resolution imaging. Traditional algorithmic methods, including iterative reconstruction techniques, face challenges in yielding accurate results under these situations. The emergence of deep learning techniques, especially convolutional neural networks (CNNs) and long short-term memory (LSTM) networks, has resulted in significant progress in image reconstruction through improved feature extraction, noise reduction, and anomaly identification. Nonetheless, current models have difficulties in thoroughly resolving the inverse problem, particularly when subtle changes in the input data require accurate capture and interpretation.

To address the previously mentioned limitations, this study introduces differential layer – a novel neural network element of architecture that improves the quality of any model (e.g., CNN, LSTM), regardless of the layer structure used in it. The proposed solution enables specialized tracking of subtle changes between parallel information flows, which ultimately facilitates more precise parameter estimation and reduces the information deficit. The central part of the architecture, which is the final layers of the model, transforms the difference into the output solution of the inverse problem under consideration. The main innovation lies in the difference layer, in which the outputs of the two branches are subtracted from each other. This approach allows the network to focus on the residuals, capturing and amplifying subtle variations in the data that are often overlooked by conventional models.

This architecture uses two parallel branches of a neural network, fed with identical input, which then process the data independently. The obtained results are passed to the differential layer, where they are subtracted, allowing the model to operate on the value resulting from the difference (residual). This quantity reflects the indeterminacy characteristic of a wide class of inverse problems. The differential architecture does not aim to replace existing models; rather, it enhances their performance. The incorporation of the differential architecture into CNNs and LSTMs has the potential to enhance the models'

capacity to discern subtle variations in input data.

In the framework of inverse problems, such tomographic reconstruction, input data usually shows noise or incompleteness. Under such conditions, the two branches can give different aspects of the absent or corrupted information top priority, resulting in complementary but different representations. Moreover affecting the differential signal is the modeling of approximation effects. Mathematical models often provide simplified versions of difficult physical systems in useful industrial environments. By stressing systematic deviations, the differential processing framework helps to reduce the effect of these approximations and guarantees the dependability and accuracy of the resulting data interpretation. By means of exploration of alternative feature spaces, the architecture can naturally inspire several possible solutions, so avoiding redundancy in data interpretation and guaranteeing a more complete knowledge of the input. This work aims to empirically confirm the hypothesis on the efficiency of the so-called differential architecture.

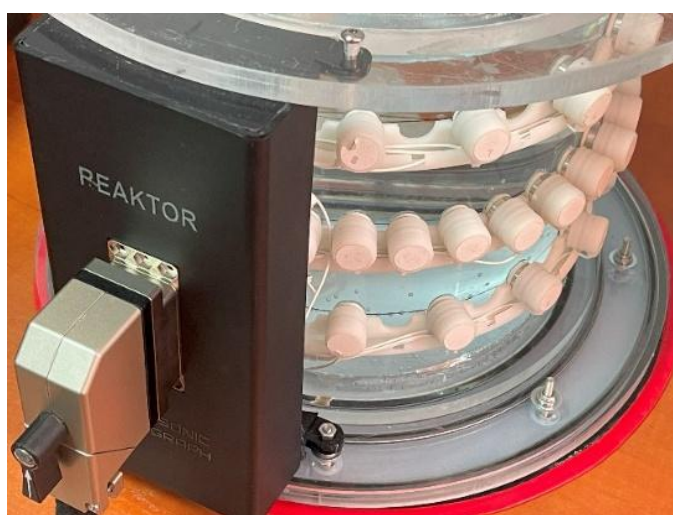
2. Materials and Methods

2.1. Hardware

At the Netrix SA research and development lab, a team developed and constructed a prototype ultrasonic tomography (UST) system for monitoring industrial processes (Figure 1).



(a)



(b)

Figure 1. UST tomograph connected to the reactor model (a), reactor model with an ultrasonic sensor system (b).

The tomography system was based on an experimental model of a water-filled reactor containing various submerged objects (Figure 2). The UST system operates by analyzing

variations in time-of-flight (TOF) measurements, which reflect the acoustic properties of the medium.

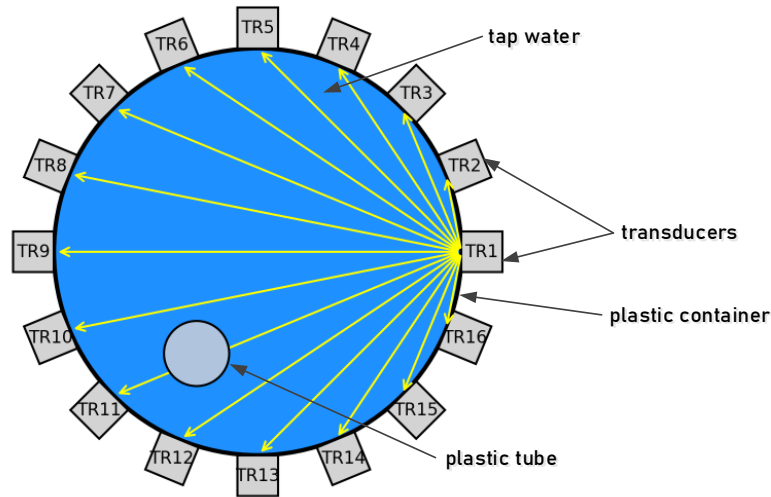


Figure 2. Cross-section of the reactor model at the height of the transducers.

The measurement apparatus utilized 16 ultrasonic transducers arranged to function in both transmission and reception modes. This configuration facilitated a thorough examination of acoustic wave propagation within the medium. The reconstruction procedure employed time-of-flight (TOF) analysis to ascertain the temporal delay of ultrasonic signals passing through several pairs of transducers. The quantity of TOF measurements was determined by the system configuration, with the total number of independent measurements adhering to equation (1). For $n = 16$ transducers, this results in exactly 120 independent measurements

$$M = \frac{n^2 - n}{2} \quad (1)$$

where n is the number of transducers. The UST system is engineered as a compact and portable device featuring sophisticated signal gathering and processing capabilities. It functions in two primary modes: full waveform mode, delivering raw data for comprehensive analysis, and transmission mode, offering processed time-of-flight and amplitude information. The lowered data size in transmission mode facilitates real-time imaging at 4 frames per second (fps), in contrast to 0.08 fps in full-waveform mode.

The system hardware is composed of 84 measurement channels, which are distributed across multiple acquisition boards. These boards are interconnected by a FD-CAN bus, which facilitates the transmission of data and the coordination of activities among all the boards. This module allows communication with a control panel via a Raspberry Pi 4B, which has a touch screen. Each transducer functions as both a

transmitter and a receiver, thereby capturing variations in acoustic wave propagation along distinct transmission paths. The strategic positioning of these transducers along the perimeter of the reactor facilitates full volumetric coverage and enables precise localization of submerged objects in a liquid medium. The system incorporates advanced signal processing electronics, including, but not limited to, a variable sampling rate analog-to-digital converter (ADC), multi-stage harmonic filtering, and programmable gain amplification. A dedicated high voltage generator produces square waveforms up to $\pm 100V$ for the purpose of optimal transducer excitation. The data acquisition unit facilitates the concurrent measurement of each excitation cycle, ensuring a high degree of data acquisition efficiency.

In order to enhance the precision of the reconstructions, reference measurements were initially conducted in an environment devoid of objects to establish a baseline for subsequent analyses. The introduction of objects into the reactor resulted in alterations to the measured TOF values, enabling the system to generate contrast-enhanced images that delineate object boundaries and spatial distributions. The UST system, which is housed in a portable enclosure, is particularly well suited for utilization in industrial environments, offering high-resolution imaging for process monitoring and anomaly detection in liquid-filled reactors.

2.2. Simulation environment

The inverse problem in UST involves estimating the internal acoustic properties of the medium from external ultrasonic data.

The primary challenge of this inverse problem stems from its ill-posed nature, allowing fluctuations in the input data to result in considerable differences in the reconstructed image. Inverse problems inherently lack uniqueness; they require mathematical regularization techniques to yield stable and physically relevant solutions. In the context of UST, the inverse problem is addressed by reconstructing a picture from limited and noisy time-of-flight measurements, a process that necessitates advanced numerical methods.

Finite element numerical simulations (FEM – finite element method) were conducted to model ultrasonic wave propagation in the reactor to overcome these problems. The FEM-based methodology produced a comprehensive depiction of acoustic wave interactions, encompassing diffraction, scattering, and multipath effects, which are essential for precise modeling of the TOF measurements utilized in picture reconstruction. The simulation environment was precisely adjusted to replicate authentic material qualities, boundary conditions, and signal distortions, thus guaranteeing that the computational model accurately represented the experimental settings.

An initial measurement was taken in an environment without objects to set a baseline TOF distribution. Then, objects were submerged into the reactor, altering the characteristics of wave propagation and resulting in TOF variations. These changes created crucial contrast for image reconstruction, allowing for the definition of object boundaries and spatial distributions.

Considering the difficulties of image reconstruction based on TOF measurements, the algorithm solving the inverse problem used a mixture of iterative reconstruction methods, regularization techniques and optimization-based strategies to obtain a stable solution. Iterative approaches such as Algebraic Reconstruction Technique (ART) and Simultaneous Iterative Reconstruction Technique (SIRT) were used to gradually increase the estimated velocity distribution. The considered reconstruction methods were updated through iterations, where these iterations were based on the differences between the actual and simulated TOF values. To further increase the stability, regularization methods such as Tikhonov regularization, which imposed a smoothness constraint to reduce noise, and Total Variation Minimization (TVM), which minimized artifacts (blurred edges, streaks, rings around objects, false signals in the

reconstruction, etc.) while preserving the edge information, were used. In addition, optimization-based approaches such as gradient descent and conjugate gradient techniques were used to minimize the discrepancy between experimental and simulated TOF. A forward finite element model allowed for an initial approximation of the TOF values, refined by iterative minimization of the error function

$$E = \sum_{i=1}^M TOF_{measured,i} - TOF_{simulated,i} \quad (2)$$

where $TOF_{measured,i}$ represents the real experimental measurements, and $TOF_{simulated,i}$ denotes the estimated values obtained from the numerical model.

The reconstruction procedure was carried out in MATLAB R2025 utilizing the EIDORS v3.12 toolbox, a renowned open-source platform for electrical and acoustic tomography. The processing steps included cleaning and adjusting the TOF data, simulating how waves move using FEM, and solving problems by repeatedly improving the reconstruction methods. This iterative approach allowed for a more accurate representation of the underlying structures, ultimately enhancing the quality of the reconstructed images. By refining the algorithms and incorporating advanced techniques, the team aimed to achieve greater precision in the tomographic results.

2.3. Data preparation for the predictive model and differential neural network architecture

To support the reconstruction of ultrasound tomographic images, a dataset of 35,000 samples was developed to simulate real-world measurement conditions. Of these, 33,000 cases were used for training, while the remaining 2,000 were reserved for testing. Each measurement vector consisted of 120 values representing the TOF differences of the ultrasound waves propagating between specific transducer pairs. Image reconstruction was performed on a high-resolution computational grid of 4,096 pixels. The reconstruction methodology was based on solving the forward problem by comparing actual TOF measurements with simulated data generated using the finite element method (FEM).

The aim of this study is to empirically verify the hypothesis regarding the effectiveness of the so-called differential architecture. The design utilizes two parallel branches of a neural network, fed with an identical input, which then process

the data independently. The results obtained from this process are then transferred to a differential layer, where they undergo subtraction. This subtraction process enables the model to operate on the value that results from the difference, also known as the remainder. This value is indicative of the vagueness characteristic of a wide class of inverse problems. It is important to note that the primary objective of this study is not to devise a novel model that will surpass other models in terms of effectiveness. Instead, the present study proposes a general mechanism of neural network architecture, termed the differential architecture, which enhances the quality of various models (e.g., CNN, LSTM), irrespective of the layer structure employed.

To verify the proposed differential mechanism, two distinct neural network structures were used: LSTM and CNN. The standard LSTM model processes the input data sequentially. The configuration of this model is shown in Figure 3. It consists of an input layer, an LSTM block, followed by a fully connected and GELU activation layer. The differential LSTM model consists of a single input layer followed by two parallel branches. Each branch contains an LSTM block. At the end of one of the branches, a Differential block with scaling layer is applied which multiplies the output values of one branch of the LSTM block by -1 . Then, the outputs of both branches are combined using an addition operation, followed by a fully connected layer and then a GELU activation layer (Table 1).

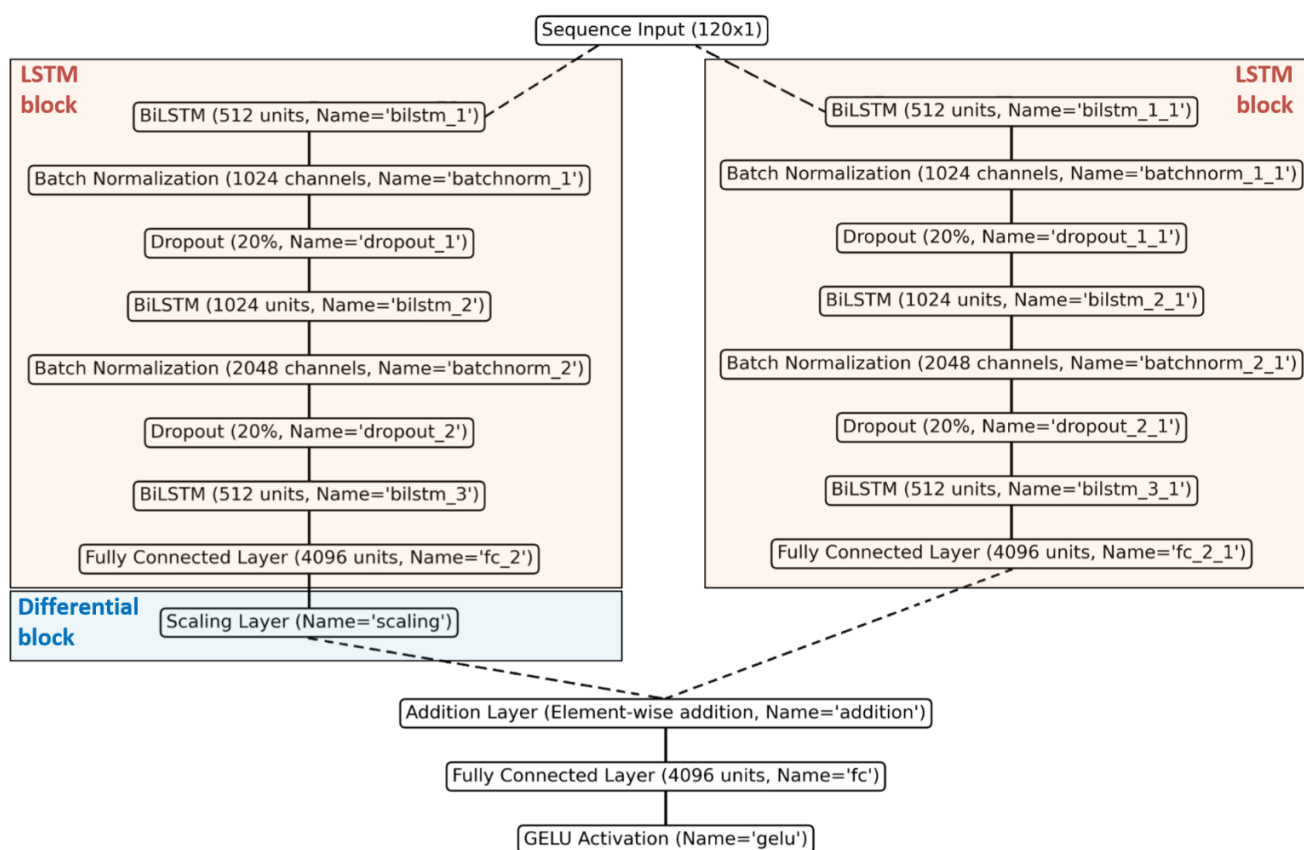


Figure 3. Layers of the differential LSTM architecture model.

Table 1. Layers of the differential LSTM architecture model.

Layer	Activations
Sequence Input with 120 dimensions	$120(C) \times 1(B) \times 1(T)$
LSTM structure block (left)	–
Scaling layer [multiply by (-1)]	$4096(C) \times 1(B)$
LSTM structure block (right)	–
Element-wise addition of 2 inputs	$4096(C) \times 1(B)$
4096ly Connected	$4096(C) \times 1(B)$
GELU	$4096(C) \times 1(B)$

The model with a CNN structure incorporates both architectures, which include a CNN structure block (see Figure 4). The standard CNN model consists of an input layer, a CNN block, a fully connected layer, and a GELU activation function. The differential CNN model comprises a single input layer, followed by two parallel branches. Each branch contains a CNN

structure block. At the end of one of the branches, a scaling layer with a factor of -1 is applied. The outputs of both branches are then combined using element-wise addition, followed by a fully connected layer and an activation function. Table 2 explains the individual layers of the differential CNN architecture model.

Table 2. Layers of the differential CNN architecture model.

Layer description	Activations
120 atures	$120(C) \times 1(B)$
CNN structure block (left)	–
Scaling layer [multiply by (-1)]	$4096(C) \times 1(B)$
CNN structure block (right)	–
Element-wise addition of 2 inputs	$4096(C) \times 1(B)$
4096ly Connected	$4096(C) \times 1(B)$
GELU	$4096(C) \times 1(B)$

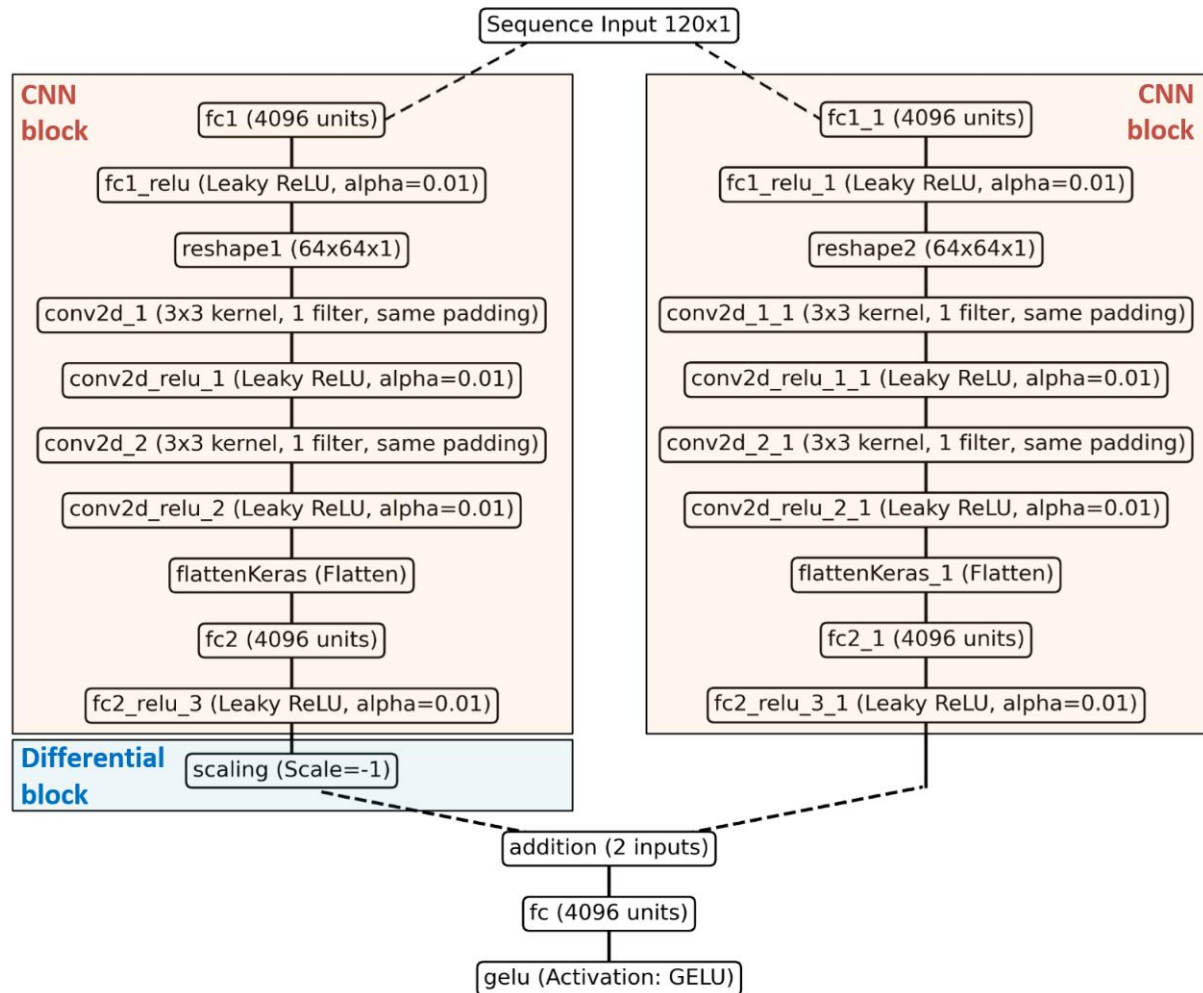


Figure 4. Layers of the differential CNN architecture model.

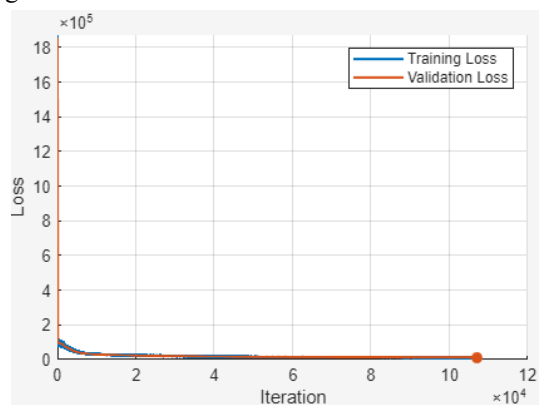
All neural networks analyzed were trained with the same parameters, which allows a fair comparison of their efficiency and the effectiveness of the training process. In the optimization process, the Adam algorithm was used to ensure that the weights

of the models were effectively adapted to the training data. Although the maximum number of training epochs was set to 3,000, an early stopping strategy was employed to prevent overfitting. Training was automatically terminated if no

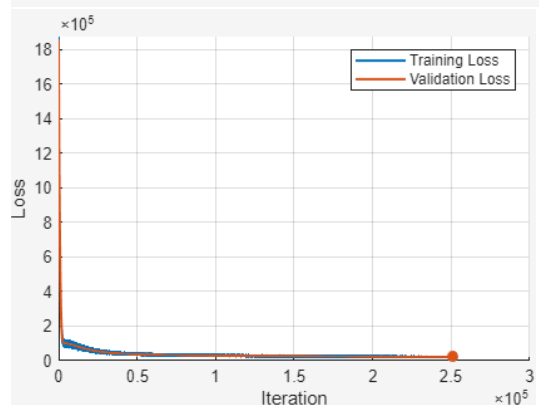
improvement in the validation loss was observed for 20 consecutive validation checks. This allowed the model to stop at the optimal point of generalization, before performance on the validation set began to degrade.

To illustrate the training dynamics, Figure 5 presents the training curves for both CNN and LSTM models, in their standard and differential variants. Each subplot shows the evolution of training and validation loss across iterations. The left column displays the full loss scale, while the right column presents the same curves with rescaled y-axes to highlight the later convergence behavior. The red markers indicate the

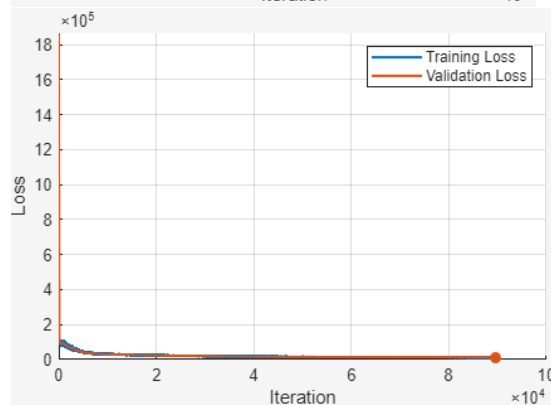
a)



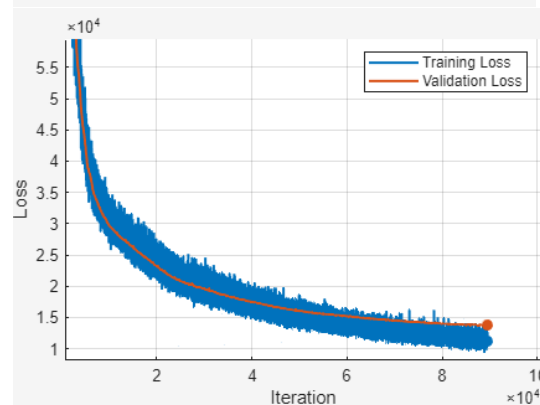
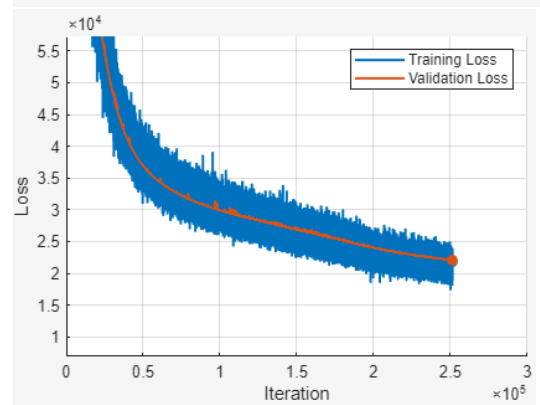
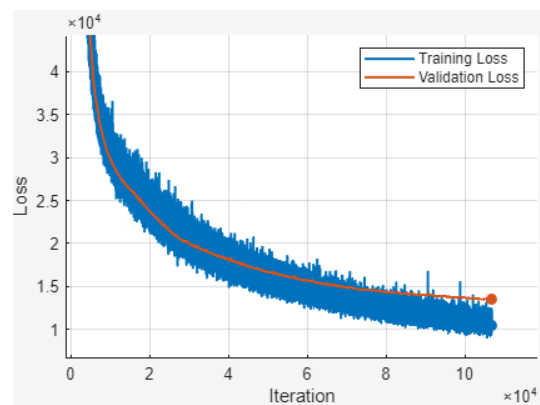
b)



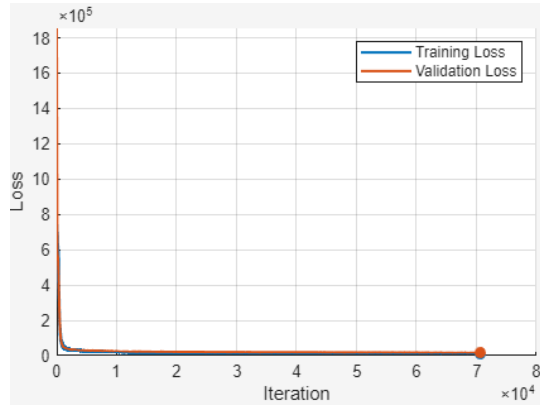
c)



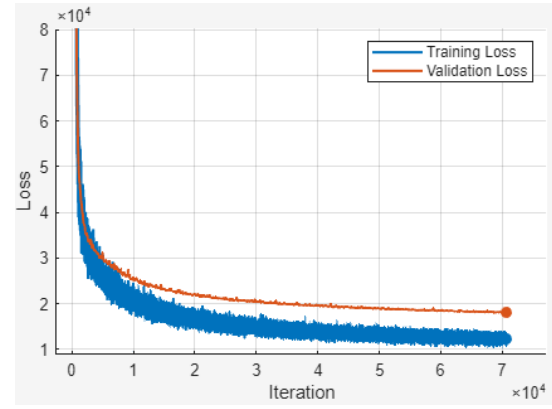
iteration at which early stopping was triggered. As seen in Figure 5a) and 5c), the differential models (LSTM and CNN, respectively) converged faster and reached lower final validation losses than their classical counterparts (Figure 5b) and 5d)). The validation loss consistently followed the training loss trend and did not increase, indicating that no overfitting occurred during training. This observation confirms the effectiveness of the regularization strategy employed and the superior generalization capability of the proposed differential architectures



d)



full graph



rescaled y-axis

Figure 5. Training and validation loss curves for: a) differential LSTM architecture model, b) LSTM model, c) differential CNN architecture model, d) CNN model.

The mini-batch size was 64, which allowed efficient use of computational resources and stabilization of the training process. The validation data were used to monitor the progress of the training, and the validation process was performed every 100 iterations, allowing a continuous evaluation of the generalization capabilities of the models. The data samples were randomly mixed at each epoch, which counteracted the memorization of sequences and improved the generalization of the models to new data.

A diverse set of quality standards (RMSE, PSNR, SSIM, and ICC) have been utilized to evaluate the precision of tomographic image reconstruction methods (refer to Table 3).

These metrics evaluate the extent to which the reconstructed image approximates the original pattern, thereby offering valuable insights into the efficacy of the underlying algorithm. The Structural Similarity Index (SSIM) is a metric that evaluates the perceived quality of a reconstructed image by taking into account structural details, brightness, and contrast variations. Conversely, the Root Mean Squared Error (RMSE) places emphasis on absolute errors. RMSE is a frequently employed metric for evaluating the precision of the reconstructed image. The computation of RMSE involves determining the mean squared intensity differences between the reconstructed and pattern images over all pixels.

Table 3. Quality indicators for the evaluation of the models received.

Quality metrics	Formula	Meaning of symbols
Root Mean Square Error (RMSE)	$RMSE = \sqrt{\frac{\sum_{i=1}^K (\hat{y}_i - y_i)^2}{K}}$	K - total number of pixels in the image y_i - the intensity of the i -th pixels in the pattern image \hat{y}_i - the intensity of the i -th pixels in the reconstructed image
Structural Similarity Index (SSIM)	$SSIM = \frac{(2\mu_{\hat{y}}\mu_y + C_1)(2\sigma_{\hat{y}y} + C_2)}{(\mu_{\hat{y}}^2 + \mu_y^2 + C_1)(\sigma_{\hat{y}}^2 + \sigma_y^2 + C_2)}$	$\mu_{\hat{y}}, \mu_y$ - the local means intensities of the reconstructed and pattern images $\sigma_{\hat{y}}, \sigma_y$ - the standard deviations of the reconstructed and pattern images $\sigma_{\hat{y}y}$ - the cross-covariance between the reconstructed and images
Peak Signal-to-Noise Ratio (PSNR)	$PSNR = 10 \cdot \log_{10}(K^2/MSE) + 50$	$C_1 = (0.01 \cdot L)^2$ and $C_2 = (0.03 \cdot L)^2$ - stabilization constants L is set to 1 for normalized pixels values in the range (0,1).
Image Correlation Coefficient (ICC)	$ICC = \frac{\sum_{i=1}^K (y_i - \bar{y})(\hat{y}_i - \bar{\hat{y}})}{\sqrt{\sum_{i=1}^K (y_i - \bar{y})^2 \sum_{i=1}^K (\hat{y}_i - \bar{\hat{y}})^2}}$	\bar{y} - the average intensity values of the pattern image $\bar{\hat{y}}$ - the average intensity values of the reconstructed image

The Peak Signal-to-Noise Ratio (PSNR) is a metric that quantifies the maximum error between the reconstructed and original images on a logarithmic scale. The conventional $PSNR_{conv}$ is defined for 8-bit images. In typical applications involving 8-bit images, PSNR values range between 30 and 50 dB, with higher values indicating superior reconstruction quality. In the context of tomographic image reconstruction, the pixel intensity values differ significantly. Specifically, the reconstructed images comprise scalar values representing distinct physical materials: 0 for water and -1 for air. This results in a limited dynamic range and includes negative values, which can lead to numerically low or even negative PSNR values when using the standard formula. To address this limitation and enhance interpretability, we introduce a constant bias term: $PSNR = PSNR_{conv} + 50$.

The Image Correlation Coefficient (ICC) is a metric that assesses the linear correlation between the pattern and reconstructed images, providing a reliable metric for evaluating the preservation of spatial distribution patterns.

3. Results and discussion

3.1. LSTM neural network

The reconstruction results from both the LSTM neural network model and the differential LSTM architecture model across five cases are presented in Table 4. The selection of five cases for the purpose of comparative analysis is outlined below. The initial column displays the reference images, the second column presents the reconstructions made using the LSTM neural network model, and the final column displays the reconstructions generated by the differential LSTM architecture. The findings reveal that the reconstructions employing the differential LSTM architecture exhibit superior detail and a more precise alignment with the reference pattern in comparison to those generated by the standard LSTM model. Additionally, the images reconstructed using the differential architecture appear sharper, which enhances the visibility of key structural elements. This finding suggests that employing a differential architecture not only improves the accuracy and reliability of the reconstructions but also provides better visual clarity.

Table 4. Results of the reconstructions using LSTM and differential LSTM architecture models.

#	Pattern	LSTM model	differential LSTM architecture model
Case #1			
Case #2			

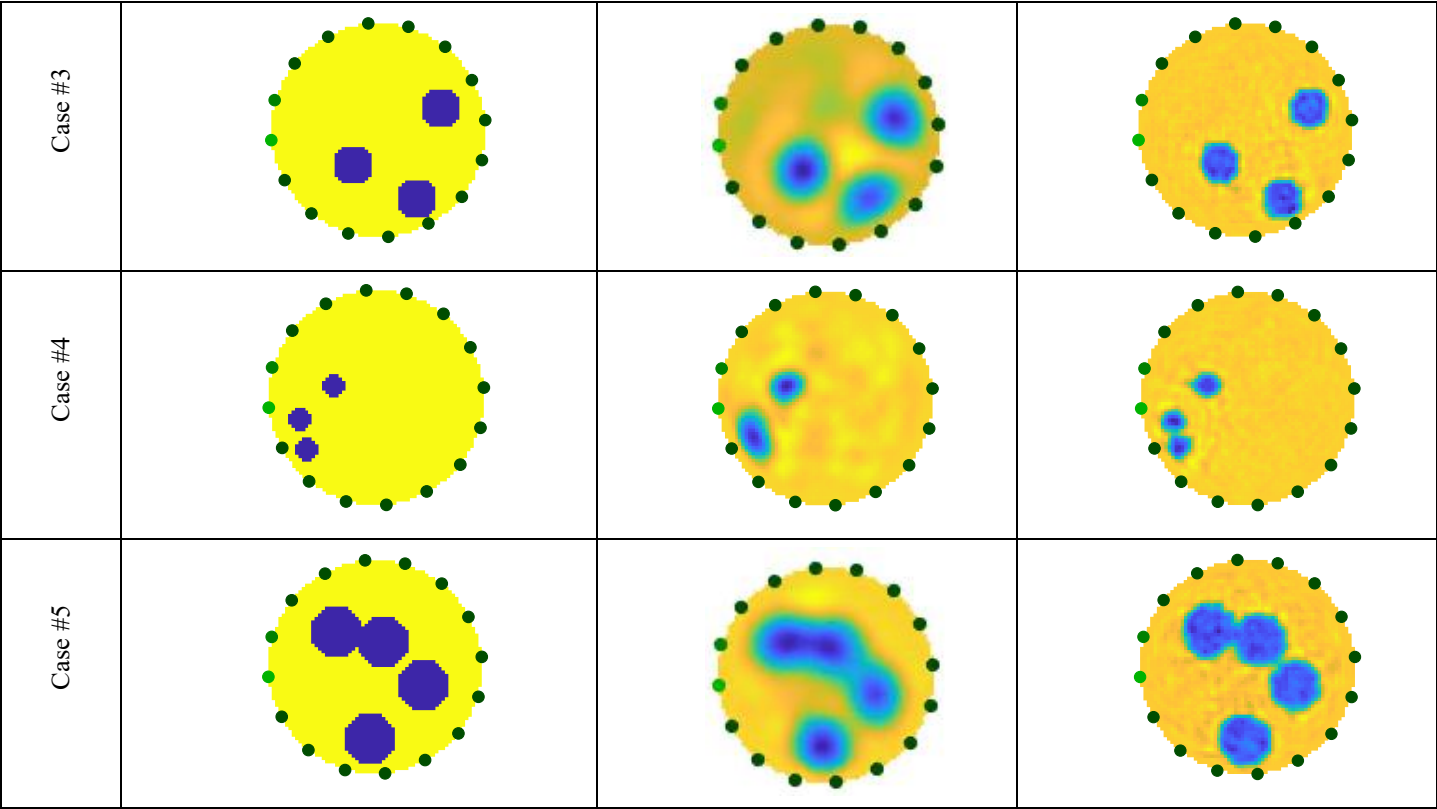


Table 5 shows a comparison of the reconstruction quality indicators from a standard LSTM model and a differential LSTM model. The columns present data related to specific cases, from Case #1 to Case #5, alongside an additional column that

displays the average quality indicators. The rows are arranged according to the quality indicators. The results for each indicator from the standard LSTM model and the differential LSTM architecture model are presented.

Table 5. Comparison of reconstruction quality indicators for LSTM models.

#		Case #1	Case #2	Case #3	Case #4	Case #5	average
RMSE	LSTM model	134.58	206.24	170.31	163.25	251.87	185.25
	differential LSTM architecture model	74.8	115.94	83.5	103.92	156.3	106.89
PSNR	LSTM model	7.42	7.31	5.37	5.74	1.98	5.56
	differential LSTM architecture model	12.52	8.72	11.57	9.67	5.63	9.62
SSIM	LSTM model	0.46	0.5	0.47	0.46	0.55	0.48
	differential LSTM architecture model	0.51	0.57	0.52	0.49	0.58	0.53
ICC	LSTM model	0.97	0.93	0.95	0.95	0.92	0.95
	differential LSTM architecture model	0.99	0.98	0.99	0.98	0.97	0.98

The analysis of the data presented in the table indicates that, with respect to RMSE, the differential LSTM model exhibits superior reconstruction quality in all test cases and in the averaged validation results. The mean RMSE for the differential model is 106.89, markedly lower than the 185.25 achieved by the regular LSTM model. The most significant improvement is observed in Case #2, where the RMSE reduced from 206.24 to 115.94, confirming the effectiveness of the differential LSTM design in error reduction. A comparable trend is noted in the PSNR metric. Elevated PSNR values signify enhanced

reconstruction quality, and the differential LSTM model achieved superior values relative to the conventional model across all test cases and in the aggregated results. The average PSNR score for the differential model is 9.62, indicating a significant improvement above the regular LSTM model's score of 5.56. The most notable discrepancy was noted in Case #3, where the differential model reached a PSNR of 11.57, in contrast to the standard model's 5.37. A further analysis of the SSIM index also indicates the superiority of the differential LSTM model. The SSIM values for the differential model

consistently surpass those of the standard model across all test scenarios and in the average validation outcomes. The mean SSIM value for the differential model is 0.53, indicating a significant improvement over the 0.48 attained with the conventional LSTM model. Case #2 exhibited the most substantial discrepancies, with the differential model achieving an SSIM value of 0.57, markedly exceeding the conventional model's score of 0.07. The ICC index further illustrates enhanced results for the differential LSTM model. Elevated ICC values indicate improved concordance and superior reconstruction quality. The differential LSTM model achieves an average ICC value of 0.98, whilst the conventional LSTM model attains a value of 0.95. The greatest significant improvement is observed in cases #2 and #5, where the ICC increased by 0.05.

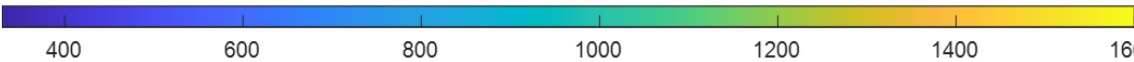
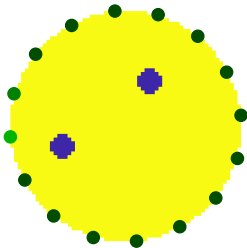
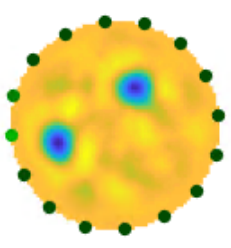
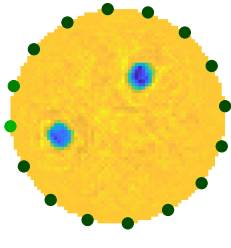
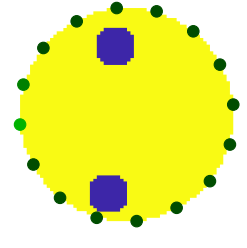
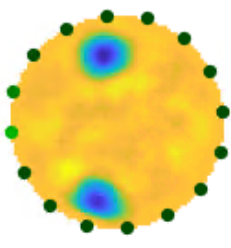
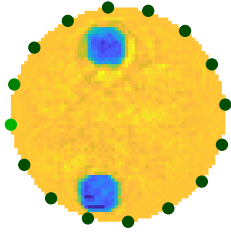
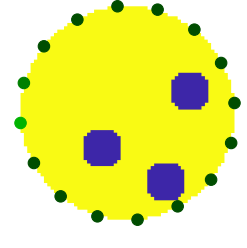
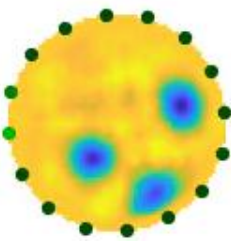
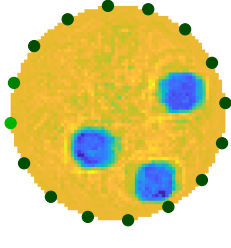
The superiority of the differential LSTM model over the standard LSTM model is evident from the results presented. The superiority is unequivocal in all examined reconstruction

quality metrics. The differential model consistently achieves superior outcomes across all test cases and exhibits a substantial advantage in the averaged results of one hundred validation cases.

3.2. CNN neural network

Table 6 shows the reconstruction results obtained using both the CNN neural network model and the differential CNN architecture model for five examples. Compared to the standard CNN model, the reconstructions made with the differential CNN architecture have more details and are more aligned with the reference pattern. In addition, as can be seen in the figures, these reconstructions appear sharper, improving the visibility of key structural elements. This suggests that the use of a differential architecture not only improves accuracy and reliability, but also provides better visual quality in the reconstructed images.

Table 6. Results of the reconstructions using CNN and differential CNN architecture models.

#	Pattern	CNN model	differential CNN architecture model
			
Case #1			
Case #2			
Case #3			

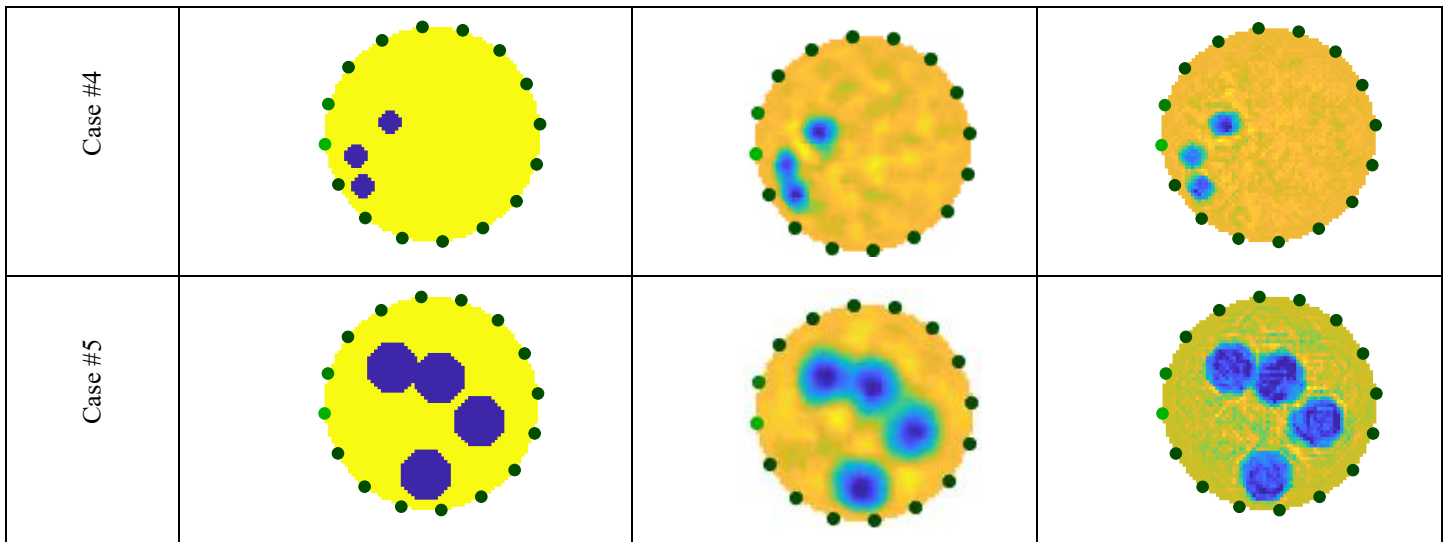


Table 7 presents, next to those of a differential CNN architecture model, the reconstruction quality indicators of a standard CNN model. The columns present details on the same five cases as for LSTM. A sixth column also includes the

average quality indicators from five validation cases. The quality measuring criteria guide the arrangement of the rows. The results of the differential CNN architecture model and the standard CNN model are presented for every indicator.

Table 7. Comparison of reconstruction quality indicators for CNN models.

Metrics and models		Case #1	Case #2	Case #3	Case #4	Case #5	average
RMSE	CNN model	140.67	178.98	156.39	202.52	220.89	179.89
	differential CNN architecture model	72.08	112.91	78.63	98.16	158.7	104.1
PSNR	CNN model	7.04	4.94	6.12	3.87	3.12	5.02
	differential CNN architecture model	12.84	7.5	12.09	9.64	5.99	9.61
SSIM	CNN model	0.43	0.46	0.43	0.41	0.52	0.45
	differential CNN architecture model	0.46	0.51	0.48	0.48	0.59	0.5
ICC	CNN model	0.98	0.95	0.97	0.96	0.94	0.96
	differential CNN architecture model	0.99	0.98	0.99	0.98	0.97	0.98

The results presented in Table 7 clearly show the superiority of the differential CNN model over the standard CNN model in all evaluated reconstruction quality indicators. The differential model is characterized by lower reconstruction error, higher PSNR, better data structure preservation according to the SSIM index, and higher reconstruction consistency with real data according to the ICC index. The average results confirm that the advantage of the differential CNN model is not random, but systematic, making it a more effective approach in the analyzed reconstruction tasks.

When applied to the inverse problem in ultrasonic tomography (UST), Figure 6 displays the average values of the reconstruction quality metrics for four model configurations: standard CNN, CNN with a difference layer (CNN Diff), LSTM with a difference layer (LSTM Diff), and standard LSTM. The information shows the mean outcomes of a thousand test cases.

Better reconstruction performance is indicated by lower values of the root mean square error (RMSE), which is displayed in panel (a). It is evident that both architectures were greatly enhanced by the difference layer. For LSTM, the RMSE drops from 190.61 to 111.70, while for CNN, it drops from 187.88 to 107.85. This evidence suggests that by lowering the error value, the subtraction operation successfully improves the model's accuracy. Better reconstruction fidelity is indicated by higher values of the peak signal-to-noise ratio (PSNR), which is displayed in panel (b). When the difference layer is added, the PSNR rises from 5.64 to 9.33 for LSTM and from 5.65 to 9.57 for CNN. These findings demonstrate that models with differences produce reconstructions of higher quality, displaying tomographic data in a clearer and more distinct manner.

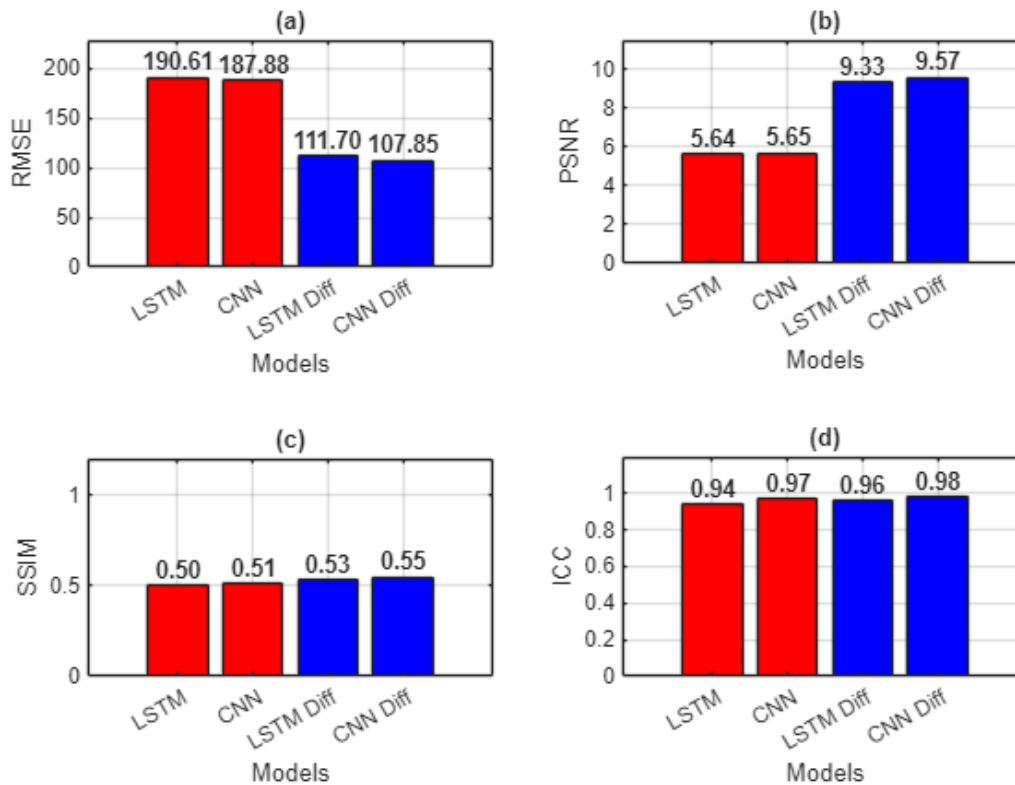


Figure 6. Average values of the metrics for LSTM vs LSTM Diff and CNN vs CNN Diff models covering 1000 test cases: (a) - average RMSE, (b) - average PSNR, (c) - average SSIM, (d) - average ICC

The Structural Similarity Index Measure (SSIM), which gauges how structurally similar the reference and reconstructed images are thought to be, is displayed in panel (c). With the difference layer, the CNN rises from 0.51 to 0.55, and the LSTM model improves from 0.50 to 0.53. This experiment demonstrates once more how the difference layer helps to improve detail preservation in UST imaging.

Lastly, the image correlation coefficient (ICC), a statistical indicator of dependability, is displayed in panel (d). After adding the difference term, the ICC rises from 0.94 to 0.96 for the LSTM architecture and from 0.96 to 0.98 for the CNN. These numbers demonstrate the reconstructed images' increased robustness and consistency across multiple samples. In conclusion, Figure 6 supports the earlier findings that the difference layer's integration into the CNN and LSTM architectures improves all assessed metrics, demonstrating its efficacy in resolving the inverse problem in ultrasound tomography.

3.3. Comparison of differential LSTM and differential CNN architectures

A comparison of the differential LSTM and differential CNN architectures reveals important differences in how well they

reconstruct, highlighting their strengths based on the type of data and the reconstruction problems that arise in certain situations. Both architectures significantly outperform their standard counterparts in all measured quality metrics, but the way they handle reconstruction differs due to their structural characteristics.

As reflected in the RMSE values, one of the most notable differences between the two architectures is how they handle error minimization. In most cases, the differential CNN model is better at reconstructing details than the differential LSTM model. This is especially true when high frequency details are important. As an example, in Case 3, the difference CNN model has a much lower RMSE than the normal CNN model. This suggests that its convolutional layers are very good at detecting spatial relationships in complicated structures. The differential LSTM model, on the other hand, is better than the standard model, but it reduces errors less significantly. This suggests that it may have problems with complex spatial dependencies, which are better handled by CNN.

The differential LSTM model does a better job of keeping signals clear and reducing noise, as shown by the PSNR values, even though CNN is better at minimizing errors. In Case #1, the

differential LSTM model reconstructs patterns more accurately than the standard LSTM, especially in areas where structural continuity is important. The differential CNN model also improves the PSNR compared to its standard version. However, the difference is more pronounced when the LSTM model makes good use of sequential dependencies.

Both architectures show improvements in their ability to maintain structural integrity as measured by SSIM. However, the CNN reconstructions tend to be sharper and more structurally coherent than the LSTM reconstructions. This effect is particularly evident in Case 5, where the differential CNN model is more effective at reconstructing fine structural elements than is the differential LSTM model. In contrast, the differential LSTM model still shows improvements over the standard version, but seems to struggle a bit more to capture intricate local details. This means that CNN's hierarchical feature extraction can help maintain structural consistency, especially when textures are complicated or there are many high-frequency changes.

The ICC values indicate that the reconstructions align well with the reference data. The differential CNN model consistently exhibits robust correlations among various cases. In Case #4, the standard CNN model exhibited a lower ICC initially; however, the differential CNN model markedly enhanced the correlation with the reference data. The differential LSTM model enhances ICC values. Nonetheless, its performance is inferior to that of the CNN-based architecture in scenarios characterized by significant structural differences, exemplified by Case #2. This indicates that although LSTM is proficient in modeling sequential dependencies, CNN is more appropriate for tasks where spatial correlations are predominant.

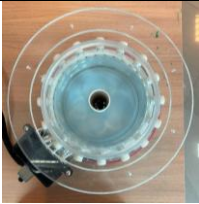
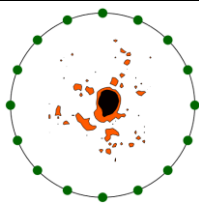
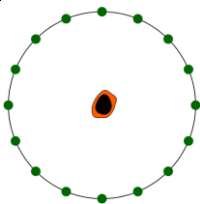
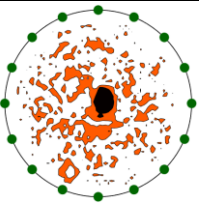
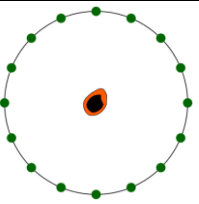
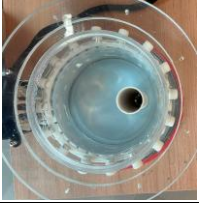
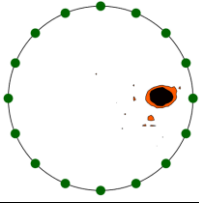
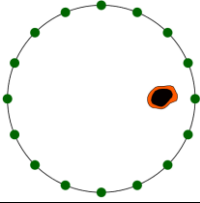
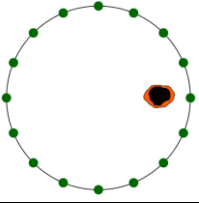
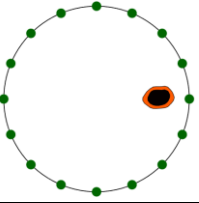
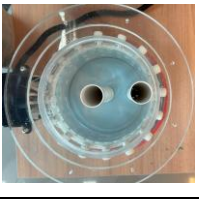
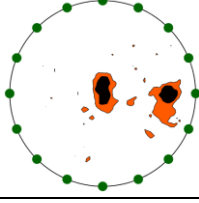
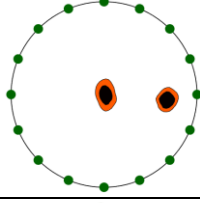
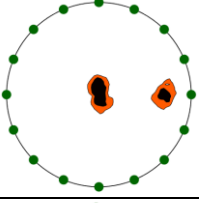
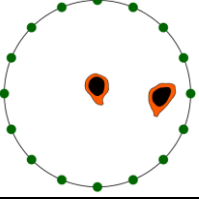

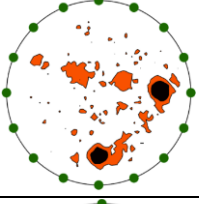
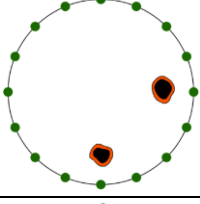
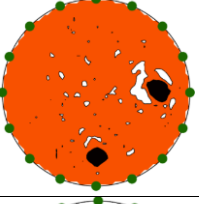
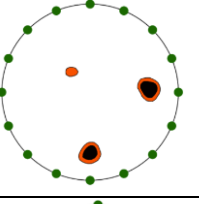
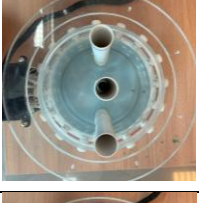
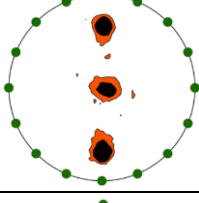
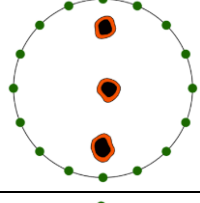
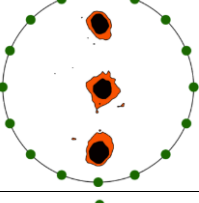
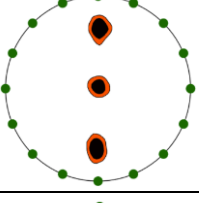
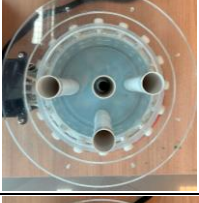
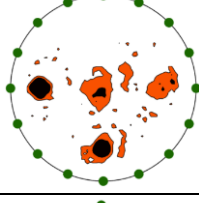
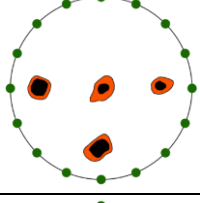
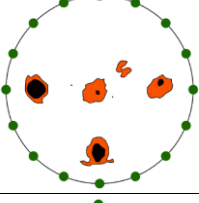
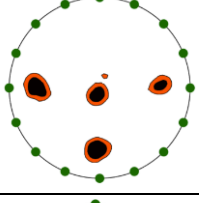

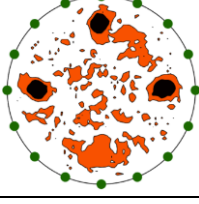
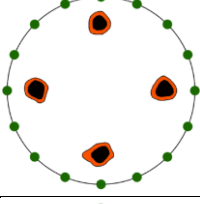
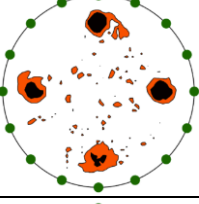
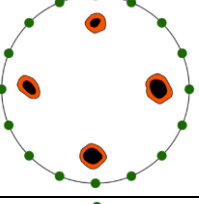

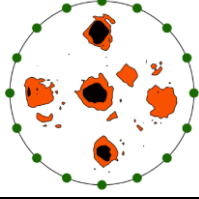
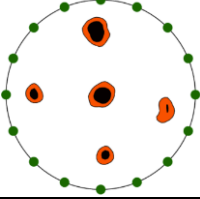
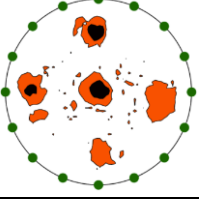
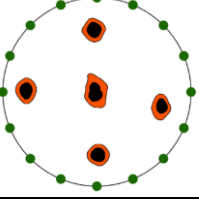
Both differential architectures significantly outperform their conventional counterparts. Nevertheless, particularly in the presence of intricate spatial connections, the differential CNN model appears superior in managing fine structural details, reducing mistakes, and preserving features. Concurrently, the differential LSTM model persists as a formidable option for applications where sequential linkages and signal continuity are paramount. The findings indicate that the selection between the two architectures ought to be determined by the characteristics of the data and the particular difficulties of the reconstruction task.

3.4. Reconstructions with real data

Table 8 compares the reconstructions obtained from real measurements using regular and differential models. The column titled "Ground Truth" contains photos from the top of the tank under investigation. The photos show different ways of arranging plastic tubes filled with air. The tubes are immersed in tap water. The tomographic reconstructions were postprocessed using the *contourf* function available in Matlab R2025. The *contourf* function serves as a tool for visualizing scalar fields defined over two-dimensional domains by generating filled contour plots. Given a scalar function $f(x, y)$, it computes isolines corresponding to specific levels c , where $f(x, y) = c$, and fills the regions between these contours with colors that represent the magnitude of f . This approach facilitates the interpretation of spatial variations in the scalar field.

Mathematically, the function operates on a grid defined by matrices \mathbf{X} and \mathbf{Y} , which specify the coordinates over the domain, and a matrix \mathbf{Z} containing the values of $f(x, y)$ at each grid point. If the contour levels are not explicitly provided, the function automatically selects them based on the range of values in \mathbf{Z} , typically dividing this range into a default number of intervals. For each specified or automatically determined level, the function interpolates between grid points to identify the contour lines and then fills the regions between these lines with colors derived from the current colormap. The resulting plot provides a continuous representation of the scalar field's magnitude across the domain. In the context of tomographic image reconstruction, the *contourf* function proves particularly beneficial during the tuning and evaluation phases. Tomographic reconstruction algorithms, such as artificial neural networks, involve iterative processes and parameter adjustments to optimize image quality. Utilizing *contourf* allows to visualize the reconstructed images' scalar fields, highlighting regions of interest, artifacts, or inconsistencies that may arise due to parameter choices. Filled contour plots can accentuate the boundaries, aiding in the assessment of reconstruction fidelity. Moreover, the ability to overlay multiple contour plots or adjust transparency settings enables comparative analyses between different reconstruction methods or parameter sets, facilitating a more informed optimization process.

Table 8. Comparison of the basic and differential models using real measurements.

#	Ground Truth	CNN	CNN diff	LSTM	LSTM diff
Case #1					
Case #2					
Case #3					
Case #4					
Case #5					
Case #6					
Case #7					
Case #8					

Reconstruction images show two color levels, obvious inclusions are marked in black. Less obvious ones are distinguishing inclusions from the background. The most marked in orange. Comparing tomographs made using LSTM

and CNN models in the classic and differential variants, it can be seen again that reconstructions made using models with differential architecture are more unambiguous. This is visible in all eight distributions studied and it does not matter whether the model used was LSTM or CNN. This proves the universality of the proposed differential concept.

4. Conclusions

This study has introduced and evaluated a novel differential neural network architecture designed to enhance the reconstruction quality in ultrasonic tomography (UST) applied to industrial reactors. By incorporating a differential layer that processes residual signals between two parallel neural network branches, the proposed architecture addresses key limitations associated with the ill-posed nature of inverse tomographic problems. This simple mechanism significantly improves the sensitivity of the model to subtle variations in input data, a feature particularly relevant to applications in process monitoring and structural diagnostics.

Empirical results derived from both simulated and real-world datasets demonstrate that the differential architecture consistently outperforms its conventional counterparts. Comparative assessments using standard metrics – RMSE, PSNR, SSIM, and ICC – indicate that both CNN and LSTM models integrated with the differential layer achieve better accuracy, structural fidelity, and robustness. In particular, the

CNN-based differential model proves more effective in resolving complex spatial patterns, while the LSTM-based counterpart shows advantages in preserving temporal coherence and reducing noise. The universality of the differential approach is confirmed by its successful application across diverse network architectures and data modalities.

The implementation of the differential mechanism has practical implications for industrial applications, where accurate and real-time reconstructions are essential for operational safety and optimization. The compact and portable UST system developed in this work, combined with the improved neural models, provides a viable solution for in situ diagnostics in reactor environments characterized by dynamic conditions and limited measurement accessibility. The differential neural network architecture represents a flexible and effective enhancement strategy for inverse problem-solving in tomography. It contributes not only to methodological advancements in imaging but also to the broader goal of increasing the reliability and efficiency of industrial process monitoring systems. Future research will focus on integrating the differential architecture with advanced deep learning models such as transformers and on extending its application to multimodal tomography. Additionally, exploring model compression techniques will be essential for real-time deployment in industrial environments with limited computational resources.

References

1. Aghajanian S, Koulountzios P, Soleimani M et al. Insights into the Application of Ultrasound Tomography in the Precipitation of Calcium Carbonate. *Chemical Engineering & Technology* 2023; 46(11): 2273–2278, <https://doi.org/10.1002/CEAT.202300213>.
2. Amrutha T. Industrial Monitoring System. *International Journal of Advanced Research in Science, Communication and Technology (IJARSCT)* International Open-Access, Double-Blind, Peer-Reviewed, Refereed, Multidisciplinary Online Journal 2024. doi:10.48175/IJARSCT-19147, <https://doi.org/10.48175/IJARSCT-19147>.
3. Arnold W, Goebbels K, Kumar A. Ultrasonic Non-destructive Materials Characterization. *Springer Series in Materials Science* 2023; 329: 1–134, https://doi.org/10.1007/978-3-662-66489-6_1.
4. Dorval V, Leymarie N, Imperiale A, Demaldent E. Multi-modal characterization of ultrasonic bulk wave properties in heterogeneous textured media through finite element computations. *Journal of Physics: Conference Series* 2024; 2904(1): 012005, <https://doi.org/10.1088/1742-6596/2904/1/012005>.
5. El-Abd M, Khanafer M, Darwiche A et al. A Machine Learning and IoT-Enabled Robot Swarm System for Pipeline Crack Detection. *IoT* 2024; (5): 951970, <https://doi.org/10.20944/PREPRINTS202411.0386.V1>.
6. Emerson J N, Marrero-Jackson E H, Nemets G A et al. Nuclear Reactor Pressure Vessel Welds: A Critical and Historical Review of Microstructures, Mechanical Properties, Irradiation Effects, and Future Opportunities. *Materials & Design* 2024; 244: 113134, <https://doi.org/10.1016/J.MATDES.2024.113134>.
7. Goncharsky A V., Romanov S Y, Seryozhnikov S Y. Artifacts of Reconstructed Images in Inverse Problems of Ultrasound Tomography in

- Models with Absorption. Lobachevskii Journal of Mathematics 2024; 45(7): 3051–3062, <https://doi.org/10.1134/S1995080224603886/FIGURES/7>.
8. Graziano F, Coppola S, Vespini V et al. Exploring the Frontiers of Non-Destructive Techniques: Shearography, Ultrasound Laser and Thermography. EPJ Web of Conferences 2024; 309: 02008, <https://doi.org/10.1051/EPJCONF/202430902008>.
9. Habib M K, Mohamed K. Machine Learning-Based Predictive Maintenance: Using CNN - LSTM network. 2023 IEEE International Conference on Mechatronics and Automation, ICMA 2023 2023: 2224–2229, <https://doi.org/10.1109/ICMA57826.2023.10216091>.
10. Hu J, Li N, Wang L et al. Direct estimation of gas holdup in gas-liquid bubble column reactors using ultrasonic transmission tomography and artificial neural processing. Measurement Science and Technology 2022. doi:10.1088/1361-6501/AC5D78, <https://doi.org/10.1088/1361-6501/AC5D78>.
11. Ji Y, Yang S, Zhou K et al. Deep-learning approach for automated thickness measurement of epithelial tissue and scab using optical coherence tomography. Journal of Biomedical Optics 2022. doi:10.1117/1.JBO.27.1.015002, <https://doi.org/10.1117/1.JBO.27.1.015002>.
12. Joshua N R, Aravind Raj S. Quality control in additive manufacturing: a review of traditional and advanced techniques. Engineering Research Express 2025. doi:10.1088/2631-8695/ADBC47, <https://doi.org/10.1088/2631-8695/ADBC47>.
13. Karapanagiotis C, Heimann J, Duffner E et al. Towards predictive maintenance of hydrogen pressure vessels based on multi-sensor data. e-Journal of Nondestructive Testing 2024. doi:10.58286/30513, <https://doi.org/10.58286/30513>.
14. Kleman C, Anwar S, Liu Z et al. Full Waveform Inversion-Based Ultrasound Computed Tomography Acceleration Using Two-Dimensional Convolutional Neural Networks. Journal of Nondestructive Evaluation, Diagnostics and Prognostics of Engineering Systems 2023. doi:10.1115/1.4062092, <https://doi.org/10.1115/1.4062092>.
15. Kłosowski G, Rymarczyk T, Niderla K et al. Using an LSTM network to monitor industrial reactors using electrical capacitance and impedance tomography – a hybrid approach. Eksploatacja i Niezawodność 2023. doi:10.17531/EIN.2023.1.11, <https://doi.org/10.17531/EIN.2023.1.11>.
16. Korzeniewska E, Sekulska-Nalewajko J, Gocłowski J et al. Evaluation of self-repair efficiency of polymers containing microcapsules using optical coherence tomography. Composite Structures 2025. doi:10.1016/J.COMPSTRUCT.2024.118525, <https://doi.org/10.1016/J.COMPSTRUCT.2024.118525>.
17. Koulountzios P, Rymarczyk T, Soleimani M. A 4-D Ultrasound Tomography for Industrial Process Reactors Investigation. IEEE Transactions on Instrumentation and Measurement 2022. doi:10.1109/TIM.2022.3164166, <https://doi.org/10.1109/TIM.2022.3164166>.
18. Kozłowski E, Borucka A, Oleszczuk P, Jałowicz T. Evaluation of the maintenance system readiness using the semi-Markov model taking into account hidden factors. Eksploatacja i Niezawodność 2023. doi:10.17531/EIN/172857, <https://doi.org/10.17531/EIN/172857>.
19. Lei M, Zhang W, Zhang T et al. Improvement of low-frequency ultrasonic image quality using an enhanced convolutional neural network. Sensors and Actuators A: Physical 2024; 365: 114878, <https://doi.org/10.1016/J.SNA.2023.114878>.
20. Levin A I, Pecherskaya E A, Shepeleva J V. et al. Problems in the Implementation of Electrical Impedance Tomography. International Conference of Young Specialists on Micro/Nanotechnologies and Electron Devices, EDM 2023; 2023-June: 1360–1363, <https://doi.org/10.1109/EDM58354.2023.10225097>.
21. Li Z, Zhang S, Dong F. Dynamic Behavior Analysis Based Process State Monitoring for Gas-liquid Two Phase Flow in Horizontal Pipe. Conference Record - IEEE Instrumentation and Measurement Technology Conference 2022. doi:10.1109/I2MTC48687.2022.9806630, <https://doi.org/10.1109/I2MTC48687.2022.9806630>.
22. Lin Z, Zhang X, Nandi P et al. Correlative single-cell hard X-ray computed tomography and X-ray fluorescence imaging. Communications Biology 2024. doi:10.1038/S42003-024-05950-Y, <https://doi.org/10.1038/S42003-024-05950-Y>.
23. Liu H, Tan C, Dong F. Absolute reconstruction of Ultrasonic Tomography for oil-water biphasic medium imaging using modified ray-tracing technique. Measurement: Sensors 2020; 7–9: 100023, <https://doi.org/10.1016/J.MEASEN.2020.100023>.
24. Liu H, Tan C, Dong F. Multi-frequency fusion ultrasonic tomography for gas-liquid two-phase distribution imaging. Measurement Science and Technology 2020. doi:10.1088/1361-6501/ABBEED, <https://doi.org/10.1088/1361-6501/ABBEED>.
25. Ma Y ;, Jiang Y ;, Li C A et al. A Universal Model for Ultrasonic Energy Transmission in Various Media. Sensors 2024; 24(19): 6230, <https://doi.org/10.3390/S24196230>.
26. Meher S S, Kakran V. Predictive Maintenance of Industrial Equipments combining IoT and Data Science Techniques using Feed Forward

- Neural Network. 2024 Control Instrumentation System Conference: Guiding Tomorrow: Emerging Trends in Control, Instrumentation, and Systems Engineering, CISCION 2024 2024. doi:10.1109/CISCION62171.2024.10696859, <https://doi.org/10.1109/CISCION62171.2024.10696859>.
27. Pennati F, Angelucci A, Morelli L et al. Electrical Impedance Tomography: From the Traditional Design to the Novel Frontier of Wearables. *Sensors* 2023; 23(3): 1182, <https://doi.org/10.3390/S23031182>.
 28. Rajpoot A K, Awasthi S, Naruka M S et al. Time Sequence Data Monitoring Method Based on Auto-Aligning Bidirectional Long and Short-Term Memory Network. A Practitioner's Approach to Problem-Solving using AI 2024: 158–170, <https://doi.org/10.2174/9789815305364124010012>.
 29. Ren J, Li J, Liu C et al. Deep Learning With Physics-Embedded Neural Network for Full Waveform Ultrasonic Brain Imaging. *IEEE Transactions on Medical Imaging* 2024; 43(6): 2332–2346, <https://doi.org/10.1109/TMI.2024.3363144>.
 30. Rzaşa M R. Selection of optical tomography parameters for gas bubble shape analysis. *Chemical and Process Engineering - Inżynieria Chemiczna i Procesowa* 2014; 35(1): 19–33, <https://doi.org/10.2478/CPE-2014-0002>.
 31. Rzaşa M R. Measurement of parameters of the moving gas bubbles with the image tomograph. 11th IMEKO TC14 Symposium on Laser Metrology for Precision Measurement and Inspection in Industry, LMPMI 2014 2014: 247–252.
 32. Shin Y, Na K Y, Kim S E et al. LSTM-Autoencoder Based Detection of Time-Series Noise Signals for Water Supply and Sewer Pipe Leakages. *Water* 2024; 16(18): 2631, <https://doi.org/10.3390/W16182631>.
 33. Sierra S, Wong J, Dawson K et al. Real Time Mechanical Integrity for Pressure Vessels and Other Critical Assets. American Society of Mechanical Engineers, Pressure Vessels and Piping Division (Publication) PVP 2022. doi:10.1115/PVP2022-84348, <https://doi.org/10.1115/PVP2022-84348>.
 34. Słoński M, Schabowicz K, Krawczyk E. Detection of flaws in concrete using ultrasonic tomography and convolutional neural networks. *Materials* 2020. doi:10.3390/MA13071557, <https://doi.org/10.3390/MA13071557>.
 35. Song J, Yan R, Lu J et al. Research on oil and gas pipeline leak detection method based on 1DCNN-DBO-LSTM. *Measurement Science and Technology* 2024; 36(1): 016024, <https://doi.org/10.1088/1361-6501/AD9047>.
 36. Sunetcioglu S, Arsan T. Predictive Maintenance Analysis for Industries. 2024 IEEE International Black Sea Conference on Communications and Networking, BlackSeaCom 2024 2024: 344–347, <https://doi.org/10.1109/BLACKSEACOM61746.2024.10646292>.
 37. Takiguchi T. Ultrasonic Tomographic Technique and Its Applications. *Applied Sciences* 2019; 9(5): 1005, <https://doi.org/10.3390/APP9051005>.
 38. Tan C, Li X, Liu H, Dong F. An ultrasonic transmission/reflection tomography system for industrial multiphase flow imaging. *IEEE Transactions on Industrial Electronics* 2019; 66(12): 9539–9548, <https://doi.org/10.1109/TIE.2019.2891455>.
 39. Wajman R. The concept of 3D ECT system with increased border area sensitivity for crystallization processes diagnosis. *Sensor Review* 2021; 41(1): 35–45, <https://doi.org/10.1108/SR-10-2019-0254>.
 40. Wajman R, Nowakowski J, Łukiański M, Banasiak R. Machine learning for two-phase gas-liquid flow regime evaluation based on raw 3D ECT measurement data. *Bulletin of the Polish Academy of Sciences: Technical Sciences* 2024. doi:10.24425/BPASTS.2024.148842, <https://doi.org/10.24425/BPASTS.2024.148842>.
 41. Wang T, Yu C. Research on ultrasonic echo signal denoising via integration of adaptive variational mode decomposition algorithm and convolutional neural network. *Insight: Non-Destructive Testing and Condition Monitoring* 2024; 66(9): 567–575, <https://doi.org/10.1784/INSI.2024.66.9.567>.
 42. Yang F, Mao Q, Shi M et al. Enhancing Ultrasound Imaging through Convolutional Neural Networks: A Health Informatics Approach. *Health Informatics and Biomedical Engineering Applications* 2024. doi:10.54941/AHFE1005073, <https://doi.org/10.54941/AHFE1005073>.
 43. Yang J, Wang F, Ren J. Noise Robust edge detection based on wavelet transform and convolutional neural networks. *ACM International Conference Proceeding Series* 2023: 691–697, <https://doi.org/10.1145/3641584.3641686>.
 44. Zamiela C, Jiang Z, Stokes R et al. Deep Multi-Modal U-Net Fusion Methodology of Thermal and Ultrasonic Images for Porosity Detection in Additive Manufacturing. *Journal of Manufacturing Science and Engineering* 2023. doi:10.1115/1.4056873/1156667, <https://doi.org/10.1115/1.4056873/1156667>.

45. Zhang K, Entezari A. Convolutional Forward Models for X-Ray Computed Tomography. *SIAM Journal on Imaging Sciences* 2023; 16(4): 1953–1977, <https://doi.org/10.1137/21M1464191>.
46. Zhang Y, Dai X, Tian Z et al. Liver motion tracking in ultrasound images using attention guided mask R-CNN with long-short-term-memory network. *Proceedings of the SPIE* 2022; 12038: 120380O, <https://doi.org/10.1117/12.2613013>.
47. Chapter 7: Mixing. In Gurugubelli S, Marabathuni V J, Sarella PNK et al. (eds): *A Text Book of Pharmaceutics for I Year Diploma in Pharmacy*, ThinkPlus Pharma Publications: 2024. doi:10.69613/R2T3QC44, <https://doi.org/10.69613/R2T3QC44>.